E. LEVEUGLE
D.S. IVANOV
L.V. ZHIGILEI[✉]

Photomechanical spallation of molecular and metal targets: molecular dynamics study

Department of Materials Science & Engineering, University of Virginia, 116 Engineer's Way,
Charlottesville, Virginia 22904-4745, USA

ABSTRACT Microscopic mechanisms of photomechanical spallation are investigated in a series of large-scale molecular dynamics simulations performed for molecular and metal targets. A mesoscopic breathing sphere model is used in simulations of laser interaction with molecular targets. A coupled atomistic-continuum model that combines a molecular dynamics method with a continuum description of the laser excitation and subsequent relaxation of the conduction band electrons is used for metal targets. Similar mechanisms of the laser-induced photomechanical spallation are observed for molecular and metal targets. For both target materials, the relaxation of compressive stresses generated under conditions of stress confinement is found to be the main driving force for the nucleation, growth and coalescence of voids in a subsurface region of an irradiated target at laser fluences close to the threshold for fragmentation. The mechanical stability of the region subjected to the void nucleation is strongly affected by the laser heating and the depth of the spallation region in bulk targets is much closer to the surface as compared with the depth where the maximum tensile stresses are generated. Two stages can be identified in the evolution of voids in laser spallation, the initial void nucleation and growth, with the number of voids of all sizes increasing, followed by void coarsening and coalescence, when the number of large voids increases at the expense of the quickly decreasing population of small voids. The void volume distributions are found to be relatively well described by the power law $N(V) \sim V^{-\tau}$, with exponent gradually increasing with time. Comparison of the simulation results obtained for Ni films of two different thicknesses and bulk Ni targets suggests that the size/shape of the target plays an important role in laser spallation. The reflection of the laser-induced pressure wave from the back surface of a film results in higher maximum tensile stresses and lower threshold fluence for spallation. As the size of the film increases, the locations of the spallation region and the region of the maximum tensile stresses are splitting apart and the threshold fluence for spallation increases.

PACS 79.20.Ds; 61.80.Az; 02.70.Ns; 83.60.Uv

1 Introduction

The role of the laser-induced stresses and associated photomechanical effects in laser ablation has been a subject of active investigations and discussions [1]. In particular, it has been demonstrated that the relaxation of the laser-induced stresses can lead to cavitation and disruption of a liquid surface region or mechanical fracture/spallation of a solid target at energy densities significantly below the ones needed to induce the explosive or even normal boiling of the material [2–6]. The ejection of large droplets or fractured solid fragments, observed both experimentally [2, 7, 8] and in simulations [9–12], as well as surface microcracking and defect accumulation [13] is often attributed to the photomechanical effects. The energetically efficient "cold ablation" driven by the relaxation of the laser-induced stresses has also been discussed as an attractive way to limit the extent of collateral thermal damage in medical applications of laser ablation [5, 14, 15].

The magnitude of the laser-induced stresses and the role of the associated photomechanical effects in material ejection depend on the relation between the laser pulse duration, τ_p, and the characteristic time of mechanical equilibration of the absorbing volume, τ_s. When the laser pulse duration is shorter or comparable with the time that is needed to initiate a collective motion of atoms or molecules within the absorbing volume, the laser heating and melting of a crystalline target takes place at nearly constant volume condition, causing a buildup of high compressive stresses. This condition, usually referred as inertial or stress confinement [1–3, 5, 9–12, 14], can be expressed as $\tau_p \leq \tau_s \sim L_p/C_s$, where C_s is the speed of sound in the irradiated material and L_p is the laser penetration depth or the size of the absorbing volume. The interaction of the laser-induced compressive stresses with the free surface of the irradiated sample can result in generation of tensile stresses sufficiently high to cause mechanical fracture of a brittle material or promote cavitation and fragmentation in a metastable liquid.

By analogy with the term "spallation," commonly used to describe the dynamic fracture that results from the reflection of a shock wave from a back surface of a sample [16, 17], the material ejection due to the laser-induced stresses is sometimes called front-surface laser spallation. While the processes of back-surface shock spallation and front-surface laser spallation are similar in their nature and can be both attributed to the interaction of an incoming compressive wave with a free surface [1], there are important distinctions in the mechanisms of material fragmentation and ejection. The mechanical stability of the front-surface region is strongly af-

[✉] Fax: +1-434/9825660, E-mail: lz2n@virgina.edu

fected by the laser heating and the mechanisms of the dynamic fracture may be rather different as compared with the back-surface spallation of a cold material. In particular, the depth of the laser-induced void nucleation and spallation observed in recent molecular dynamics (MD) simulations is found to be defined by the balance between the tensile stresses that are increasing with depth and the decreasing thermal softening of the material due to the laser heating [10, 12]. As a result, the spallation takes place significantly closer to the surface than the depth at which the maximum tensile stresses are reached. Moreover, in the case of crystalline targets, the relaxation of the laser-induced pressure proceeds on the same time scale as the laser melting [18, 19] and the interaction of the pressure wave with the melting front should be taken into account. These observations indicate that the discussion of the microscopic mechanisms and parameters of laser front-surface spallation cannot be based on a direct application of the solutions of the thermoelastic wave equation [1, 3–5] or conclusions derived from back-surface spallation experiments [16, 17]. An analysis of photomechanical damage and spallation should involve an adequate description of the interplay of the relaxation of the thermoelastic stresses, melting front propagation and homogeneous nucleation of liquid regions as well as void nucleation, growth and coalescence at elevated temperatures.

The relative contribution of photomechanical effects to the onset of material ejection can also be strongly affected by the thermodynamic and mechanical properties of the target material. While there is solid evidence of a photomechanical character of cavitation and energetically efficient ablation in simple molecular systems and aqueous solutions [2–4, 6, 9, 10, 12], the evidence for other materials is less conclusive. In many cases, the contribution of photomechanical stresses may be intertwined with other processes, such as explosive boiling, photochemical reactions in organic systems or optical breakdown plasma generation in dielectrics. Both the fast nucleation and growth of vapor bubbles in explosive boiling [20] and the release of products of photochemical reactions [21] can create a significant pressure in the surface region of the target and lead to the material ejection. These processes can proceed with or without the assistance of thermoelastic stresses, which contribute to the material ejection under conditions of stress confinement. In particular, it has been observed in MD simulations of molecular systems that larger and more numerous clusters with higher ejection velocities are produced by the explosive phase decomposition in the regime of stress confinement as compared with a simulation performed at the same laser fluence in the regime of thermal confinement [9, 12]. Moreover, the tensile stresses generated in the regime of stress confinement can bring the system deeper into the metastable region and induce the nucleation and growth of vapor bubbles at fluences at which no homogeneous boiling takes place without the assistance of thermoelastic stresses [4, 15].

While the terminology in the field of laser ablation is still being established and different terms are often used interchangeably, we will follow the discussion given in a recent review by Paltauf and Dyer [1] and use terms "photomechanical ablation" or "laser front-surface spallation" to describe the ablation mode in which the transient thermoelastic stresses

play the dominant part, with negligible contribution of the vapor phase. Photomechanically assisted explosive boiling described above, when the release of the vapor phase is the main driving force responsible for the material ejection, does not fall into the category of spallation even though the conditions for the stress confinement are satisfied and the initial thermoelastic stresses contribute to the material ejection and affect the parameters of the ejected plume. Similarly, we will use terms "cavitation" or "void formation" to describe photomechanical ablation/spallation, in contrast with the "bubble formation" in the explosive or normal boiling. Note that, in the case of crystalline targets, an ultrafast melting or other phase transformations occurring under conditions of stress confinement can make, in addition to the thermoelastic stresses, a significant contribution to the buildup of the initial stresses in the target.

In this paper, we present the results of a computational analysis of the role of the photomechanical effects in the onset of laser ablation in two drastically different types of material, an amorphous molecular solid and a crystalline metal target. The differences in the structure and thermodynamic parameters of the two target materials allow us to elucidate the general and material-specific characteristics of the photomechanical effects. The reported results are also relevant to a more general question on the microscopic mechanisms of the dynamic ductile fracture under conditions of ultrahigh strain rate and elevated temperature. The paper is organised as follows. Computational models used in simulations of laser interaction with molecular and metal targets are described in Sect. 2. The results of the simulations are presented and discussed in Sects. 3 and 4 for molecular and metal targets, respectively. An overall picture of laser-induced photomechanical effects and front-surface spallation, emerging from the simulations, is reviewed in Sect. 5.

2 Computational models for laser interaction with molecular systems and metals

2.1 *Mesoscopic model for molecular systems*

The simulations of laser ablation of an organic target are performed using the breathing sphere model that is described in detail elsewhere [22]. Briefly, the model adapts a coarse-grained representation of molecules by particles with real translational degrees of freedom, but an approximate representation of the internal degrees of freedom. The parameters of interparticle interaction are chosen to reproduce the van-der-Waals interaction in a molecular solid with cohesive energy of 0.6 eV, elastic bulk modulus of ~ 5 GPa and density of $1.2 \, \mathrm{g/cm^3}$. A mass of 100 Daltons is attributed to each molecule. The model provides an adequate description of molecular excitation by laser irradiation, intermolecular energy transfer, as well as the collective molecular dynamics induced by laser irradiation, e.g. [9–12].

In the present study, we use the breathing sphere model to perform a detailed analysis of the evolution of photomechanical damage and spallation in a molecular target. Although the ejection of a layer of relatively intact material has been reported and attributed to photomechanical effects [9, 10], a detailed analysis of the microscopic mechanisms of laser spallation has not been performed so far. A relatively small

lateral size of computational cells used in earlier simulations precluded a reliable analysis of the evolution of the voids in the spallation region. In the present work, a significantly larger computational cell with dimensions of $40 \times 40 \times 90$ nm (1 015 072 molecules) is used. The size of the computational cell remains significantly larger as compared with the largest void in the system up to the final stage of the spallation involving void coalescence and separation/ejection of a layer of material. This makes us confident that the periodic boundary conditions imposed in the directions parallel to the surface do not have a significant effect on the early evolution of the photomechanical damage.

The laser irradiation is simulated by vibrational excitation of molecules that are randomly chosen during the laser pulse duration. The probability of a molecule being excited is modulated by Lambert–Beer's law to reproduce the exponential attenuation of the laser light with depth, with an absorption depth of 50 nm. The vibrational excitation is modeled by depositing a quantum of energy equal to the photon energy into the kinetic energy of internal motion of a given molecule. Irradiation at a wavelength of 337 nm (3.68 eV) is simulated in this study. The total number of photons entering the model during the laser pulse is determined by the laser fluence. The value of the laser pulse duration, 15 ps, is chosen in order to make sure that the simulations are performed in the regime of stress confinement for which spallation and ejection of a layer of material can be expected. At the bottom of the MD computational cell we apply the dynamic boundary condition developed to avoid artifacts due to reflection of the laser-induced pressure wave from the boundary of the computational cell. The boundary condition accounts for the laser-induced pressure wave propagation as well as the direct laser energy deposition in the boundary region [12, 23].

2.2 Combined continuum-atomistic model for laser interaction with metal targets

The simulations of laser interaction with metal targets are performed with a hybrid computational model that combines the classical MD method for simulation of nonequilibrium processes of laser melting, damage and ablation with a continuum description of the laser excitation and subsequent relaxation of the conduction band electrons [18]. The model is based on the so-called two-temperature model (TTM) [24], which describes the time evolution of the lattice and electron temperatures, T_l and T_e, respectively, by two coupled nonlinear differential equations. In the combined TTM-MD method, MD substitutes the TTM equation for the lattice temperature. The diffusion equation for the electron temperature, T_e, is solved by a finite difference method simultaneously with MD integration of the equations of motion of atoms, Fig. 1. The electron temperature enters a coupling term that is added to the MD equations of motion to account for the energy exchange between the electrons and the lattice. The cells in the finite difference discretization are related to the corresponding volumes of the MD system and the local lattice temperature is defined for each cell from the average kinetic energy of thermal motion of atoms. The expansion, density variations, and, at higher fluences, disintegration of the irradiated target predicted in the MD part of the model are accounted for in the
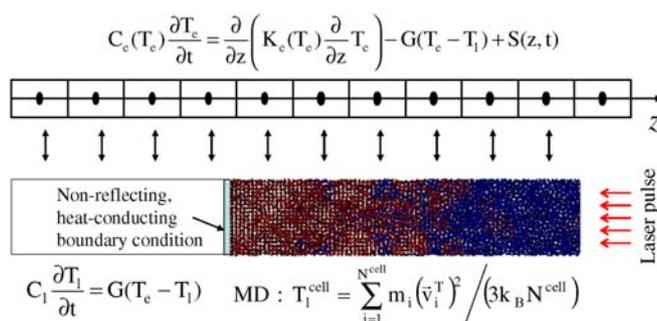

$$C_e(T_e)\frac{\partial T_e}{\partial t} = \frac{\partial}{\partial z}\left(K_e(T_e)\frac{\partial}{\partial z}T_e\right) - G(T_e - T_l) + S(z,t)$$

$$C_l\frac{\partial T_l}{\partial t} = G(T_e - T_l) \qquad MD: T_l^{cell} = \sum_{i=1}^{N^{cell}} m_i\left(\bar{v}_i^T\right)^2 \bigg/ \left(3k_B N^{cell}\right)$$

FIGURE 1 Schematic representation of the combined continuum-atomistic model for simulation of laser interaction with a metal target. The evolution of electron temperature is described by a nonlinear differential equation, whereas the atomic motions are described by the MD method with additional forces that account for the energy exchange due to the electron–phonon coupling. Spatial discretization in the continuum model (typically ~ 1 nm) and size of the atomistic region are not drawn to scale. The cells in the finite difference discretization are related to the corresponding volumes of the MD system and the local lattice temperature is defined for each cell from the average kinetic energy of thermal motion of atoms. The thermal velocity is defined as $\bm{v}_i^T = \bm{v}_i - \bm{v}^c$, where $\bm{v}_i$ is the actual velocity of an atom i and $\bm{v}^c$ is the velocity of the center of mass of a cell to which atom i belongs. A Gaussian temporal profile, $S(z,t)$, is used to describe the laser excitation of the conduction band electrons. A complete description of the combined TTM-MD model and the nonreflecting boundary condition is given in [18] and [23], respectively

continuum part of the model. A complete description of the combined TTM-MD model is given elsewhere [18].

Nickel, a transition metal with strong electron–phonon coupling and a relatively small thermal diffusivity (as compared with other metals) is used in the simulations. The strong electron–phonon coupling in Ni leads to a rapid transfer of the absorbed energy to the lattice and confines the initial laser energy deposition in a shallow surface region of the target. The energy confinement allows for a realistic simulation of laser interaction with a bulk target with a MD computational cell of only 100 nm in depth, as demonstrated in Sect. 4.

All the thermal and elastic properties of the lattice, such as the lattice heat capacity, elastic moduli, the coefficient of thermal expansion, melting temperature, volume and entropy of melting and vaporization, as well as the dependence of these characteristics on temperature and pressure are defined by the interatomic interaction, described in this work by the embedded-atom method (EAM) in the form suggested in [25]. The pressure dependence of the equilibrium melting temperature, determined from liquid-crystal coexistence simulations, as well as the equation of state of the EAM Ni material, determined in a series of constant pressure–constant temperature simulations are reported in Reference [18]. The parameters used in the continuum part of the model (TTM equation for the electron temperature) are as follows [26]. The electronic heat capacity is $C_e = AT_e$ with $A = 1065\,\mathrm{J\,m^{-3}\,K^{-2}}$, the thermal conductivity of the electrons is $K_e = K_0 T_e/T_l$ with $K_0 = 91\,\mathrm{W\,m^{-1}\,K^{-1}}$, the electron–phonon coupling constant is $G = 3.6 \times 10^{17}\,\mathrm{W\,m^{-3}\,K^{-1}}$ and the optical absorption depth is $L_p = 13.5$ nm.

In order to investigate the dependence of the photomechanical effects from target geometry/dimensions, simulations are performed for three different systems, 50 nm and 100 nm free-standing films and a bulk Ni target. The initial MD system used in the simulations of laser irradiation

of 50 nm Ni films is an FCC crystal composed of 56 800 atoms with lateral dimensions of 3.53×3.53 nm and periodic boundary conditions imposed in the directions parallel to two (100) free surfaces. A similar computational cell is used for 100 nm films, with 113 600 atoms and lateral dimensions of 3.53×3.53 nm. Simulations of laser interaction with bulk targets were performed for two sizes of the MD part of the combined TTM-MD model, $1.77 \times 1.77 \times 99.94$ nm (28 300 atoms) and $7.06 \times 3.53 \times 99.94$ nm (226 400 atoms). The continuum part of the combined TTM-MD model extends by 500 nm beyond the back end of the MD computational cell, Fig. 1, providing an adequate representation of the electronic heat conduction into the bulk of the target. Before applying laser irradiation, all systems are equilibrated at 300 K.

By comparing the results of the simulations obtained for systems with different sizes in the lateral (parallel to the surface) directions, we find that, while the general mechanisms of film damage and disintegration are not affected by the lateral sizes of the MD cell, the threshold fluences for disintegration/spallation are slightly lower for smaller computational cells due to the effect of the periodic boundary conditions. Moreover, a reliable quantitative analysis of the microscopic mechanisms of the photomechanical damage and spallation (e.g. evolution of the void size distribution) can be only performed for sufficiently large systems, where the largest void is still significantly smaller than the size of the computational cell.

3   Photomechanical spallation of a molecular target

The conditions leading to photomechanical damage and spallation, as well as the spatial and time evolution of the void distributions, are investigated in this section for two large-scale MD simulations. The first simulation is performed at a laser fluence of $31\,J/m^2$, just above the threshold for laser spallation; the second simulation is performed at a laser fluence of $25\,J/m^2$, below the threshold for laser spallation. With the laser pulse duration of 15 ps and the laser penetration depth of 50 nm, the condition for stress confinement is satisfied in both simulations. We start from a detailed analysis of the simulation performed at $31\,J/m^2$, in which spallation does occur.

The temporal and spatial evolution of the lattice temperature, pressure and density in the surface region of the irradiated bulk molecular target is shown in the form of contour plots in Fig. 2. The initial temperature increase during and immediately after the 15 ps laser pulse is related to the rapid energy transfer from the internal energy of excited molecules to the thermal energy of the translational motion of molecules. The probability of molecular excitation follows the Lambert–Beer's law and leads to the exponential decrease of the deposited energy density with depth. As a result, a strong temperature gradient is established during the first ~ 20 ps in the surface region of the molecular target, Fig. 2a. The following temperature evolution is mainly defined by the dynamics of the pressure relaxation and evolution of the photomechanical damage (void nucleation and growth). Thermal conduction to the bulk of the molecular target is slow and has only a minor effect on the temperature evolution on the timescale of 130 ps shown in Fig. 2. The two main factors
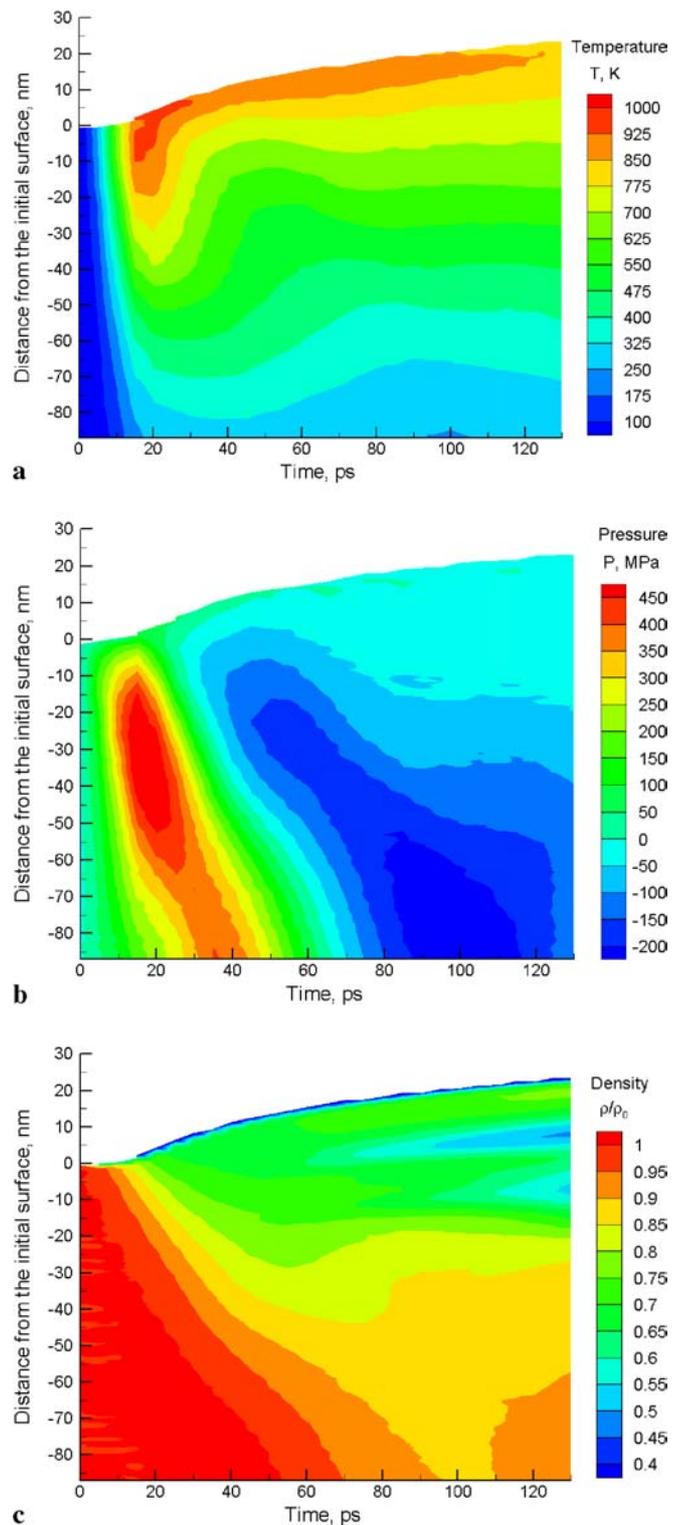

FIGURE 2 Contour plots of temperature (**a**), pressure (**b**) and density (**c**) for MD simulation of laser spallation of a molecular target. The laser pulse duration is 15 ps, optical penetration depth is 50 nm and fluence is $31\,J/m^2$. Density scale is normalised to the initial density before the irradiation, ϱ_0. Snapshots from this simulation are shown in Fig. 3. Laser pulse is directed along the Y axes, from the top of the contour plots

that are responsible for the temperature changes are discussed below.

First, the relaxation of the laser-induced pressure has a significant effect on the temperature evolution. The time of the

temperature increase in the surface region of the irradiated target is shorter than the time needed for the expansion of the absorbing region and the laser heating takes place under the condition of inertial stress confinement [9, 10]. The heating under the condition of the stress confinement results in the build up of high, up to 530 MPa, compressive pressure, Fig. 2b. The initial pressure relaxes by driving a strong compression wave into the bulk of the target, followed by a tensile component of the wave that results from the interaction of the compressive stresses with the free surface of the target. The amplitude of the tensile component of the pressure wave is increasing with depth and reaches a maximum value of -250 MPa at approximately one laser absorption depth (50 nm) beneath the surface. The maximum tensile stresses are limited by the dynamic tensile strength of the material and are lower as compared with what one would expect for a thermoelastic material response. Comparison of the temperature and pressure contour plots, Fig. 2a and b, suggests that there is a direct correlation between the pressure and temperature variations. Propagation of the tensile wave leads to a pronounced transient cooling of the material. Similar temperature–pressure correlations have been recently observed and discussed for simulations of laser interaction with metal films [18, 19]. Considering a fast adiabatic/isentropic compression or expansion of a material, the temperature vari-ation with pressure can be estimated from classical thermodynamics, $(\partial T/\partial P)_S = VT\alpha/C_P > 0$, where the heat capacity C_P, volume V and the volume coefficient of thermal expansion α are all positive for the model molecular material.

The second factor responsible for the fast temperature decrease in the surface region of the target is the onset of photomechanical damage, when the kinetic energy of thermal motion of molecules is transferred into the potential energy associated with generation of voids and eventual disintegration of the material. The first notion of the onset of photomechanical damage can be obtained from the density plot shown in Fig. 2c. Two layers of reduced density can be readily identified in the contour plot. The appearance of the first layer at ~ 55 ps at a depth of ~ 10 nm is followed by the appearance of the second layer at ~ 70 ps at a depth of ~ 27 nm. The appearance and growth of the two low-density layers can be qualitatively related to the analytical prediction on the formation of multiple spall planes in laser spallation [27]. Quantitative parameters of the photomechanical damage, such as the location of the spall layers and the distribution of voids in the surface region, however, cannot be correctly predicted by the simple spallation model. MD simulations provide a unique opportunity to perform a detailed microscopic analysis of the appearance and evolution of voids in laser spallation.
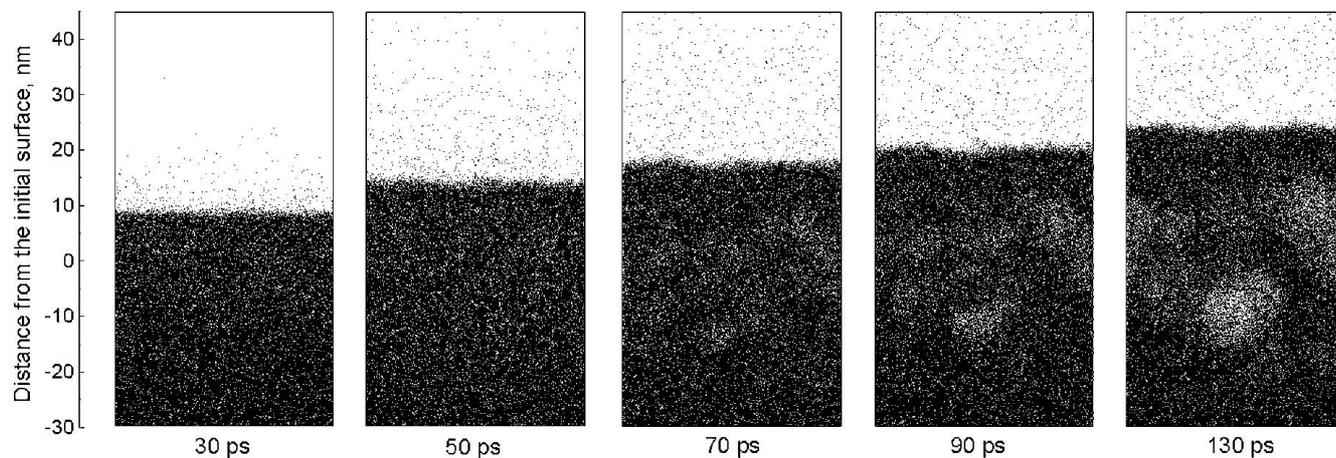

FIGURE 3 Snapshots from the simulation of laser-induced void nucleation and spallation in the regime of stress confinement. The laser pulse duration is 15 ps, optical penetration depth is 50 nm and fluence is 31 J/m². Molecules are shown by *dots* that are smaller than their actual size so that the largest voids (or regions of reduced density) could be identified in snapshots for 70, 90 and 130 ps while looking through the 40 nm-deep computational cell
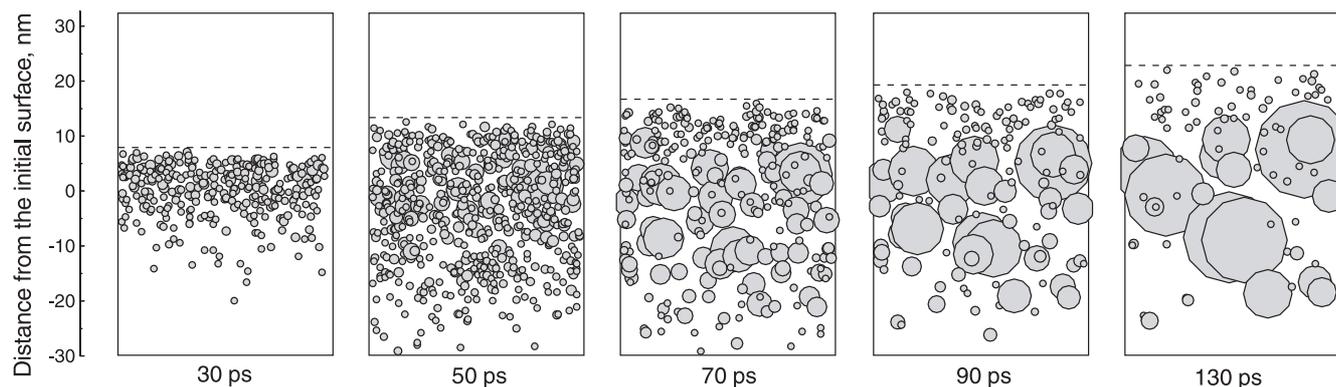

FIGURE 4 Nucleation and growth of subsurface voids in the simulation for which snapshots are shown in Fig. 3. Voids are represented by spheres of the same volume as the actual voids. *Horizontal dashed lines* show the current location of the surface

A series of snapshots from the simulation are shown in Fig. 3, where each dot corresponds to a molecule. The appearance and growth of several regions of reduced molecular density can be identified in snapshots taken at 70 ps, 90 ps and 130 ps. In order to give a clearer picture of the evolution of void distribution in the target, we use a different representation in Fig. 4, where each void is represented by an individual sphere of the same volume as the actual void. The voids are defined by superimposing molecular configuration with a three-dimensional grid of cubic cells with a size of 0.68 nm and identifying cells that do not contain any molecules. Voids are defined as clusters of more than two empty cells connected with each other by sharing a face. The choice of the parameters in the above analysis is optimised to give the best agreement with an intuitive definition of voids in a visual analysis of thin slices of the molecular configurations observed in the simulations. The appearance of large numbers of small voids in the first two snapshots shown in Fig. 4 corresponds to the expansion of the surface region of the irradiated target and can be correlated with the propagation of the tensile component of the pressure wave, Fig. 2b. At 50 ps, we can also observe the appearance of larger voids at a certain depth under the surface. At later times, the number of small voids is steadily decreasing whereas large voids continue to grow and coalesce. At a time of 130 ps, a few large voids account for the largest part of the empty volume in the subsurface region of the target. At this time, we also observe a significant deviation of the shapes of the voids from the spherical representation adapted in Fig. 4. Further development of the system leads to the void percolation and ejection of large clusters.

Quantitative information on the void evolution is presented in Figs. 5 and 6. The total volume fraction of the voids as a function of depth under the surface is shown in Fig. 5. The initial expansion of the very surface region results in a concentration of small voids near the surface and a monotonous decrease of the fraction of the empty volume with depth under the current surface at 30 ps. As the material expands further, the fraction of voids decreases in the very sur-
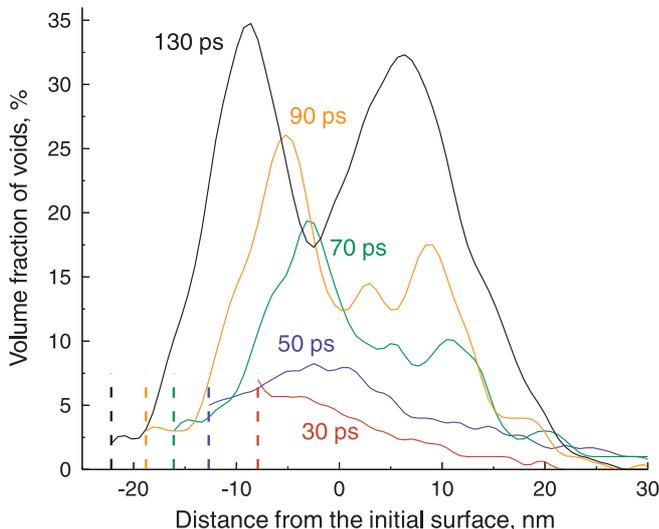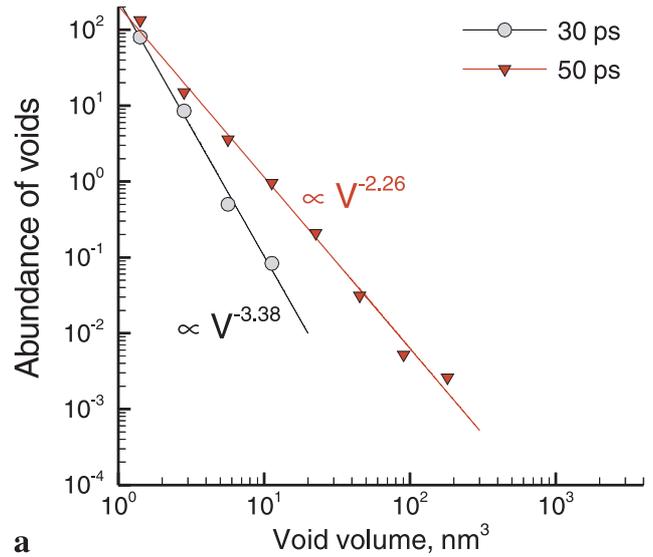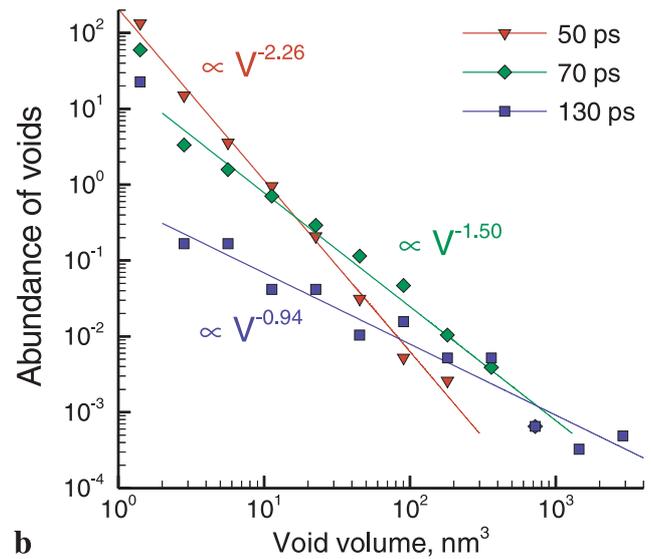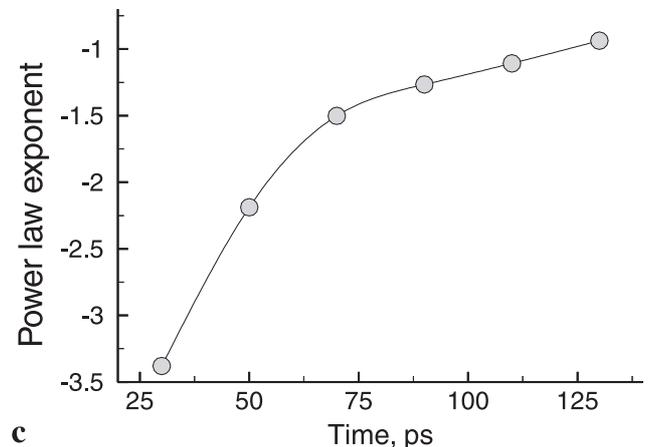
FIGURE 5   Volume fraction of voids as a function of depth under the surface of a molecular target irradiated with 15 ps laser pulse at a fluence of 31 J/m². *Vertical dashed lines* show the current location of the surface

FIGURE 6   Void abundance distributions as a function of void volume in a molecular target irradiated by a 15 ps laser pulse at a fluence of 31 J/m². Distributions are shown for 30 and 50 ps (**a**) and 50, 70 and 130 ps (**b**) after the beginning of the laser pulse. The *lines* in **a**,**b** are power law fits of the data points with the exponents indicated in the figures. Time dependence of the power-law exponents is shown in **c**

face region but a well-defined maximum develops at ~ 10 nm under the current surface position at 50 ps. This maximum shifts to ~ 13 nm below the current surface by the time of 70 ps and remains at this depth at 90 ps and 130 ps. At the same time, a second maximum starts to develop at a depth of ~ 27 nm under the current surface at 70 ps and becomes comparable with the first maximum by the time of 130 ps. This analysis can be correlated with the density contour plot discussed above, Fig. 2c, where the appearance and growth of two low-density spallation regions can be readily identified.

Figure 6 shows the void volume distributions at different times after the irradiation. Two distinct stages can be identified in the evolution of the distributions. The initial stage of void nucleation and growth is illustrated in Fig. 6a. The size distribution of voids that appear by the time of 30 ps can be well described by a steep power law with an exponent of -3.38, with no voids exceeding 13 nm^3 in volume. Both the number of voids and the range of volumes are increasing by the time of 50 ps. The distribution becomes less steep, with an exponent of -2.26 resulting from the power law fit of the data points. The second stage of void coarsening and coalescence is illustrated in Fig. 6b. From 50 ps to 70 ps, the number of large, ≥ 20 nm^3, voids increases at the expense of smaller voids. From 70 ps to 130 ps, the number of small voids continues to decrease, but very large voids appear as a result of coalescence of smaller voids. The maximum void volume steadily increases with time from 12.6 nm^3 at 30 ps to 183.4 nm^3 at 50 ps, to 817.3 nm^3 at 70 ps, to 1482.1 nm^3 at 90 ps, to 2251.7 nm^3 at 110 ps and to 3016.6 nm^3 at 130 ps. With the omission of the smallest voids, the void volume distributions at longer times can be still described by the power law with an exponent increasing with time, Fig. 6c.

Snapshots from another large-scale MD simulation performed at a lower laser fluence of 25 J/m^2, below the threshold for laser spallation, are shown in Fig. 7. Similar to the simulation discussed above, the depth of the appearance of small voids at 30 ps and 50 ps follows the propagation of the tensile component of the pressure wave. The tensile stresses, however, are not sufficient to cause further growth of the voids. The largest void, that appears at the depth of ~ 22 nm, reaches its maximum volume of 30 nm^3 at 75 ps and then decreases in size and collapses. Interestingly, the depth of the largest void growth and collapse is close to the depth

of the second spallation region in the simulation performed at a higher fluence and discussed above. As discussed before [9, 10], the depth of the most active void growth and spallation is determined by the balance between the tensile stresses, which are increasing with depth and reach their maximum at approximately one penetration depth beneath the surface (50 nm in these simulations), and the decreasing thermal softening of the material due to the laser heating. In the simulation illustrated in Fig. 7, the temperature of the region of material where the largest void is observed, ~ 22 nm, is exceeding the melting temperature of the model molecular solid only for a very short period of time at ~ 20–30 ps and the evolution of the void is taking place at a temperature close to the melting temperature.

Simulation results for molecular systems discussed above suggest that thermoelastic stresses generated in the surface region of the irradiated target under conditions of stress confinement are primarily responsible for the observed void nucleation, growth, coalescence, and eventual ejection of large chunks of material. According to the definition discussed in the Introduction, the mechanism of the energetically efficient material ejection in this case can be, therefore, called laser spallation. The relevance of this mechanism to laser interaction with metals is discussed in the next section.

4   Photomechanical spallation of a metal target

The difference in the nature of interatomic bonding between molecular systems and metals does not allow us to extrapolate the results obtained for molecular systems to metals even at a qualitative level. While the van-der-Waals interaction in a molecular solid can be relatively well represented by a pair intermolecular potential, the strength of individual bonds in metals has a strong dependence on the local environment. Pair potentials significantly, up to 2–3 times, underestimate the ratio between the cohesive energy and the melting temperature of metals and cannot account for a much stronger bonding of atoms near surfaces and in small clusters due to the localization of the electron density. Another consequence of the environmental dependence of the interatomic bonding in metals is a significantly lower vapor pressure characteristic of liquid metals as compared with molecular systems or Lennard–Jonesium, commonly used in "generic" MD
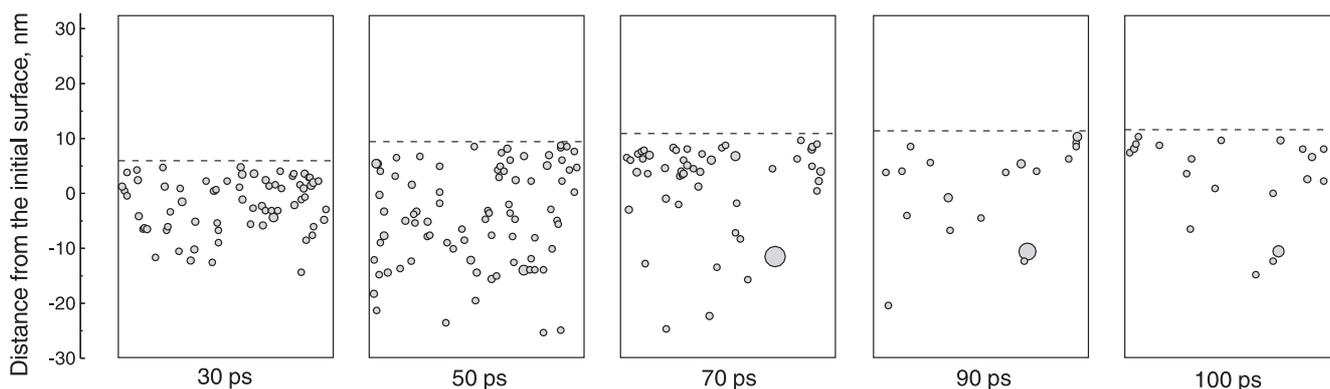
FIGURE 7   Evolution of subsurface voids in the simulation performed at a laser fluence of 25 J/m^2, below the threshold for laser spallation. Voids are represented by spheres of the same volume as the actual voids. *Horizontal dashed lines* show the current location of the surface

simulations [28, 29]. In order to investigate the relevance of the spallation mechanism to laser interactions with metals, we perform a series of simulations with a combined TTM-MD model described in Sect. 2.2. The environmental dependence of interatomic interaction in metals is correctly accounted for by EAM potential [25, 30] used in the MD part of the model.

Preliminary results of our simulations performed for 50 nm free-standing Ni films [18] suggest that the photomechanical spallation mechanism is also operational in metals. The temperature and pressure distributions in a Ni film irradiated by 1 ps laser pulse at a fluence of 860 J/m², just above the threshold for disintegration of the film, is shown in Fig. 8. The solid line in the contour plots separates the crystalline and melted parts of the film, as defined by the local order parameter described in Reference [18]. The ultrafast melting process proceeds by a homogeneous nucleation of liquid regions inside the crystalline material and is strongly affected by the dynamics of the relaxation of the laser-induced pressure, as discussed in detail in References [18, 19]. The initial temperature increase in the film, Fig. 8a, is defined by the energy transfer from the excited electrons to the lattice. Strong electron–phonon coupling in Ni leads to the steep rise of the lattice temperature during the first $\sim 5-10$ ps after the laser pulse, whereas the fast electronic heat conduction redistributes the deposited laser energy throughout the whole 50 nm film before the electron–phonon equilibration. The time of the lattice heating is shorter than the time needed for the 50 nm film to expand in response to the thermoelastic stresses and the condition of stress confinement is satisfied in the central part of the film. The heating under the condition of stress confinement results in the buildup of high, up to 11.5 GPa, compressive pressure, Fig. 8b.

The relaxation of the compressive pressure leads to the expansion of the film and generation of the tensile stresses, which reach −9 GPa close to the middle of the film, at the depth of 31 nm and time of 21 ps. The tensile stresses are sufficient to cause disintegration of the film into two large and one small pieces moving apart from each other, as indicated by the two white gaps that develop in the contour plots after ~ 30 ps, Fig. 8. The disintegration interrupts the electronic heat conduction among the pieces of the film and the final temperatures of the front and the back pieces are different by more than 500 K. Analysis of the atomic configurations during the simulation indicates that the disintegration process proceeds by the nucleation, growth, and coalescence of voids in the central part of the film, where the maximum tensile stresses are generated. The temperature of the region of the void nucleation remains below the boiling temperature and no gas-phase atoms are observed inside the growing voids, pointing to the mechanical nature of the disintegration process. Photomechanical damage/disintegration of finite-size absorbers have been observed in experiments [31] as well as in other MD simulations [29, 32–34]. The small size of the absorbing structure facilitates photomechanical disintegration, which can be partially attributed to the focusing of the unloading tensile waves propagating from the surfaces of the absorber. To study the role of photomechanical effects in thicker films and bulk metal targets, we performed a series of simulations for 100 nm Ni films and bulk Ni targets. The laser pulse of 1 ps was used
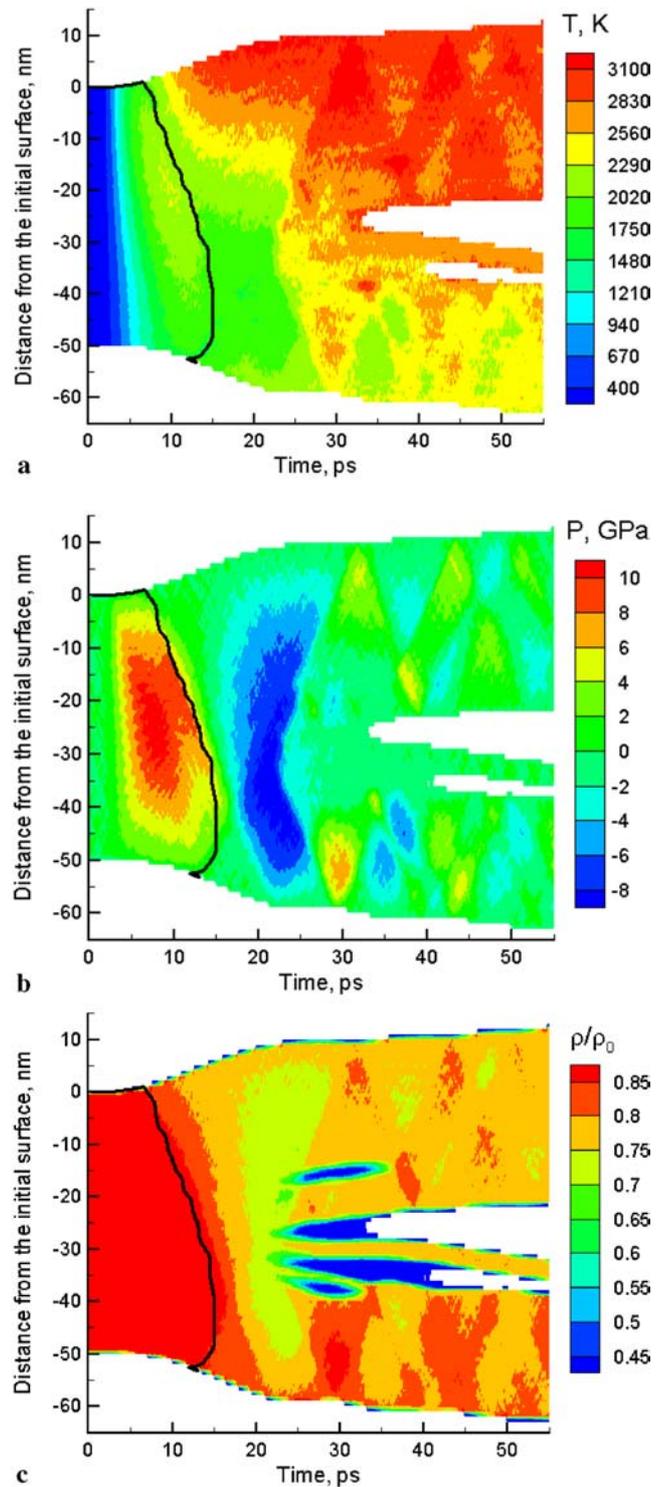

FIGURE 8 Temperature (**a**), pressure (**b**) and density (**c**) contour plots for simulation of laser melting and spallation of a 50 nm free-standing Ni film irradiated with a 1 ps laser pulse at an absorbed fluence of 860 J/m². Laser pulse is directed along the *Y*-axes, from the top of the contour plots. *Black line* separates the melted region from the crystalline part of the target. Density scale is normalised to the initial density before the irradiation, ϱ_0. Areas where the density of the material is less than $0.1\varrho_0$ are not shown in the plots

in all simulations, whereas fluence was varied to identify the thresholds for target disintegration.

The threshold fluence for disintegration of 100 nm film is found to be between 1075 J/m² (no film disintegration ob-

served) and 1290 J/m², significantly higher as compared with 50 nm films (no disintegration at 645 J/m², disintegration at 860 J/m²). The temperature and pressure contour plots for the simulation performed at 1290 J/m² for 100 nm film are shown in Fig. 9. A relatively small, as compared with other
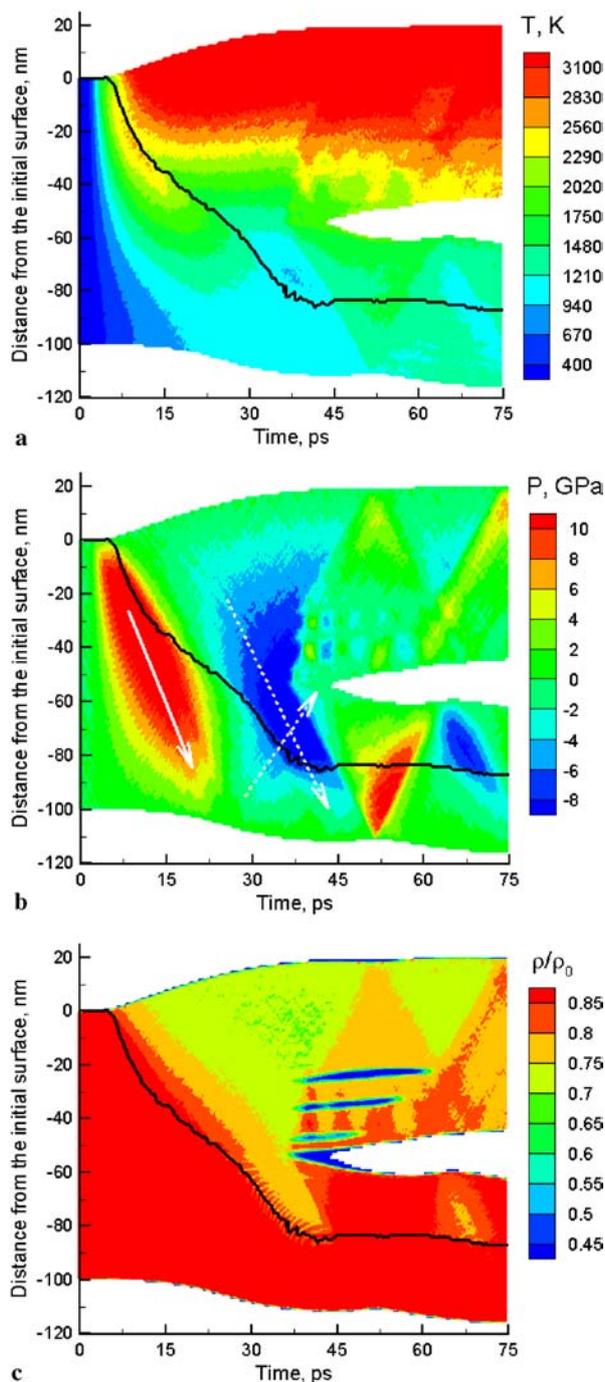

FIGURE 9 Temperature (**a**), pressure (**b**) and density (**c**) contour plots for simulation of laser melting and spallation of a 100 nm free-standing Ni film irradiated with a 1 ps laser pulse at an absorbed fluence of 1290 J/m². Laser pulse is directed along the *Y*-axes, from the top of the contour plots. *Black line* separates the melted region from the crystalline part of the target. Density scale is normalised to the initial density before the irradiation, ϱ_0. Areas where the density of the material is less than $0.1\varrho_0$ are not shown in the plots. *Solid and dashed arrows* in **b** show the directions of the compressive and tensile waves propagation, respectively

metals, thermal diffusivity and strong electron–phonon coupling in Ni leads to the initial localization of the deposited laser energy in the part of the film adjacent to the irradiated surface. The temperature increase leads to the compressive pressure buildup which, in turn, relaxes by driving a compressive pressure wave toward the back surface of the film (solid white arrow in Fig. 9b) and inducing an unloading tensile wave that follows the compressive component (dashed white arrow in Fig. 9b). The compressive pressure wave transforms into a tensile one upon reflection from the back surface (another dashed arrow in Fig. 9b). The two tensile waves superimpose with each other, generating high tensile stresses up to −11.5 GPa in a region located at a depth of ∼ 70 nm at a time of ∼ 38 ps. The maximum tensile stresses observed at the threshold for spallation in 100 nm film are significantly higher as compared with the ones that lead to disintegration of a 50 nm film, as can be seen from the plots of the maximum compressive and tensile stresses observed in simulations performed at different laser fluences, Fig. 10. In the case of 100 nm films, the maximum tensile stresses are realised farther away from the irradiated surface, where the temperature is lower, 9a and b, and the material can support higher tensile stresses. Note that, in the simulations performed for 100 nm films, the region of void nucleation and spallation is shifted toward the irradiated front surface of the film with respect to the depth where the maximum tensile stresses are created. In particular, in the simulation illustrated in Fig. 9c, the voids appear, grow and/or collapse in a wide region located at a depth of ∼ 25–55 nm, whereas the tensile stresses reach the maximum at a depth of ∼ 70 nm.

The threshold fluence for the separation of a layer from a bulk Ni target is found to be between 1720 J/m² (no layer ejection) and 1935 J/m², more than twice higher than the threshold for disintegration of a 50 nm film and ∼ 50% higher than the one for 100 nm. There is no reflection of the compressive and tensile components of the laser-induced pressure wave, which propagates through the nonreflecting boundary at the bottom of the MD part of the combined atomistic-continuum model, Fig. 11b. An abrupt decrease of the amplitude of the tensile component of the pressure wave upon crossing the crystal-liquid interface is related to the confinement of the heated crystalline material in the lateral directions. For a typical laser spot diameter of ∼ 100 μm, the fast relaxation of the laser-induced pressure can only proceed in the direction normal to the surface. These conditions of lateral confinement are correctly reproduced by the periodic boundary conditions used in the directions parallel to the surface. In the melted part of the target, the stresses remain isotropic during the uniaxial expansion of the surface region and the pressure is defined only by the volume and temperature. The uniaxial expansion of the crystalline part of the target, however, results in anisotropic lattice deformations and corresponding anisotropic stresses. The anisotropic stresses in a crystal cannot relax by uniaxial expansion and the unloading pressure wave crossing the liquid–crystal interface superimpose with the residual stresses in the crystalline part of the target, Fig. 11b. The residual compressive stresses remain in the crystalline part of the target long after the relaxation of the transient thermoelastic stresses in the melted part.
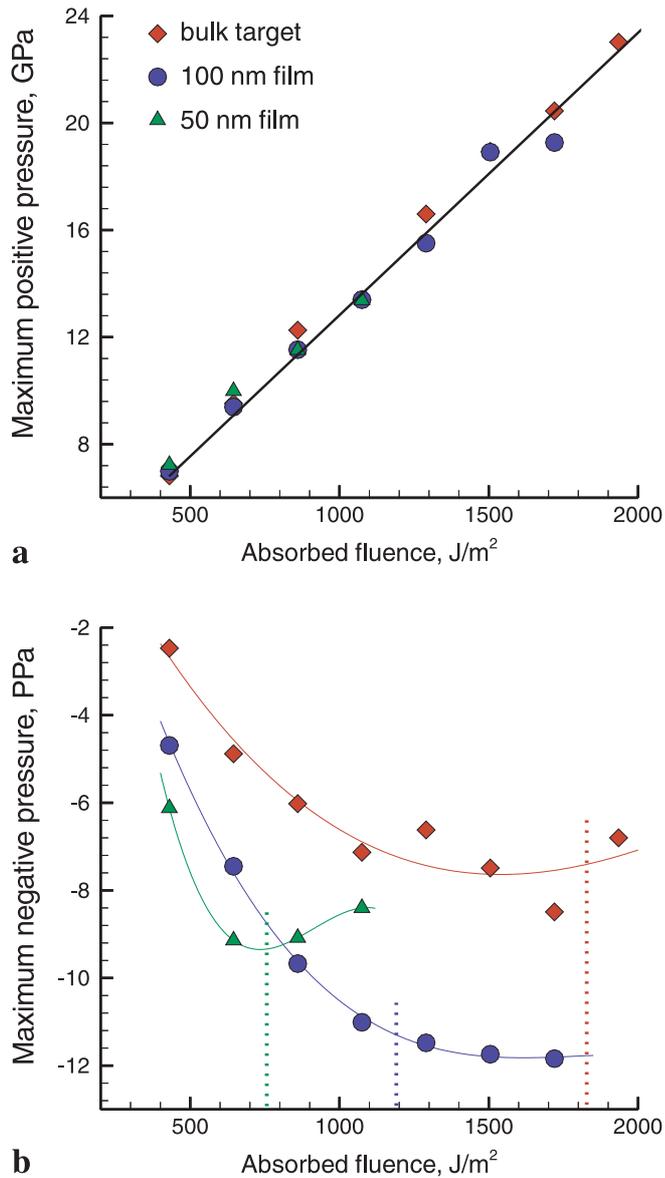
FIGURE 10 Maximum positive (compressive) and negative (tensile) pressure observed in simulations of laser irradiation of 50 nm and 100 nm free-standing Ni films and bulk Ni targets. The *dashed vertical lines* mark approximate values of thresholds for laser spallation in the simulations performed for 50 nm films (*green line*), 100 nm films (*blue line*) and bulk target (*red line*). Laser pulse duration is 1 ps in all simulations. *Solid lines* are just guides to the eye

FIGURE 11 Temperature (**a**), pressure (**b**) and density (**c**) contour plots for simulation of laser melting and spallation of a surface region of a bulk Ni target irradiated with a 1 ps laser pulse at an absorbed fluence of 1935 J/m². Laser pulse is directed along the *Y*-axes, from the top of the contour plots. *Black line* separates the melted region from the crystalline bulk of the target. *Red line* in **a**,**b** and *blue line* in **c** separates the MD and continuum parts of the combined TTM-MD model. In the current version of the model, we do not calculate pressure in the continuum part of the model but the energy of the pressure wave entering the continuum part is accounted for. The electronic heat conduction to the bulk of the target is followed in both parts of the model and a seamless connection of the temperature field in the MD and continuum parts of the model can be seen in **a**. Density scale is normalised to the initial density before the irradiation, ϱ_0. Areas where the density of the material is less than $0.1\varrho_0$ are not shown in the plots. Snapshots from this simulation are shown in Fig. 12

Similar to the results for the bulk molecular system discussed in Sect. 3 as well as the results for Ni films discussed above, the appearance of several low-density regions can be identified in the density contour plot shown in Fig. 11c. The appearance of the low-density regions coincides with the arrival of the unloading tensile wave that propagates from the surface and increases its strength with depth. All but one low-density region disappear shortly after their emergence, whereas the deepest one continues to grow and eventually leads to the separation of a ~ 25 nm-thick layer from the target. The atomic-level picture of the evolution of the low-density region is shown in Fig. 12. A number of voids appear in the subsurface region of the target at ~ 30 ps, the time when the tensile component of the pressure wave passes through the
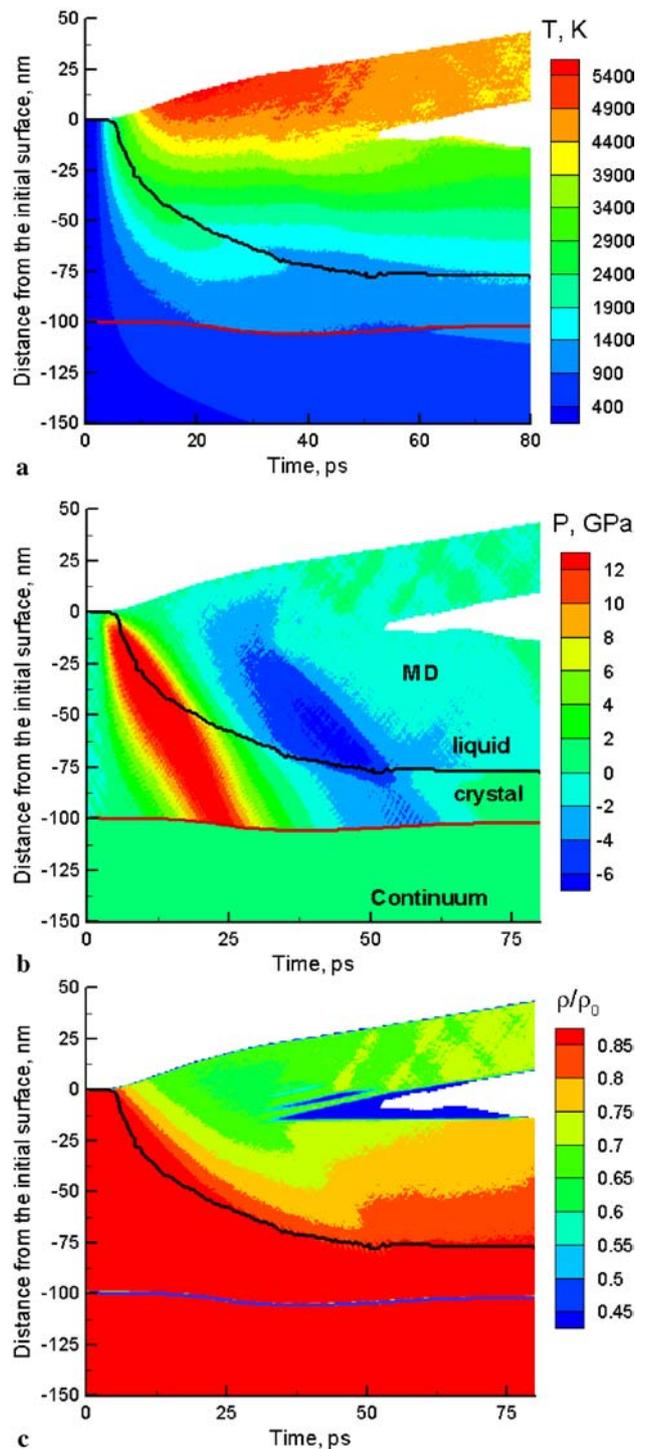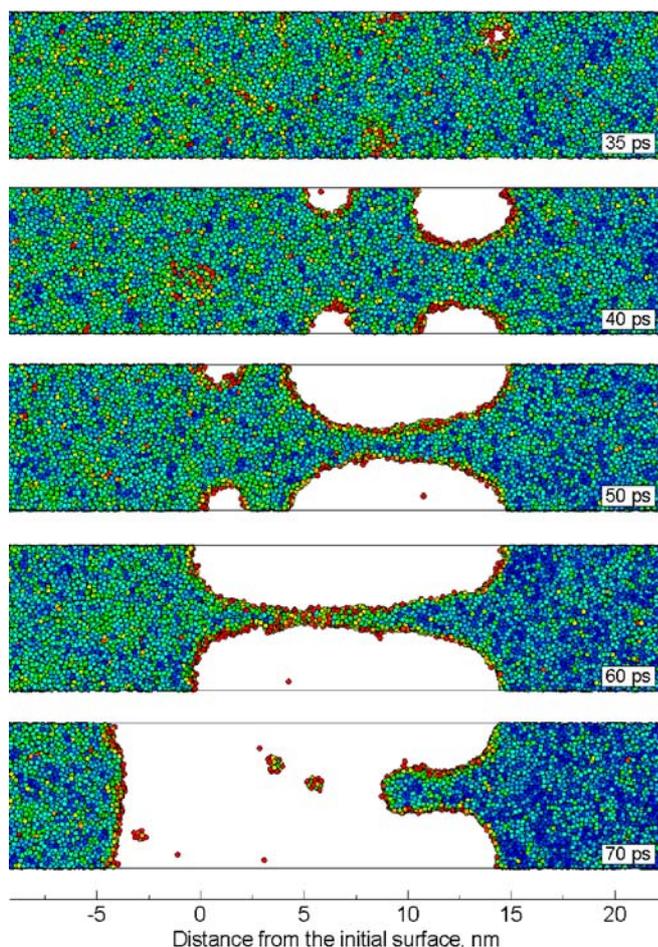
FIGURE 12 Snapshots from simulation of a bulk Ni target irradiated with a 1 ps laser pulse at an absorbed fluence of 1935 J/m². Atoms are coloured according to their potential energy (red colour corresponds to high potential energy of -2.5 eV, blue colour corresponds to low energy of -4 eV, the cohesive energy of the EAM Ni fcc crystal is 4.45 eV)

region. Some of the voids collapse, others grow, coalesce and eventually lead to disintegration of the film. Only several gas-phase atoms are observed inside the growing voids, indicating that the process of void nucleation and growth is not related to boiling but has a mechanical nature. In the simulations of disintegration of the 50 nm and 100 nm films, performed at lower laser fluences and illustrated in Figs. 8 and 9, the maximum temperatures in the regions of the void nucleation are even lower, and no gas phase atoms are observed inside the voids. We can conclude that photomechanical spallation caused by the relaxation of the laser-induced thermoelastic stresses is responsible for the onset of material fragmentation in all the simulations discussed above.

5   Discussion and summary

The results of molecular dynamics simulations of laser interaction with molecular and metal targets suggest that photomechanical spallation is a general mechanism that can be operational in a wide class of materials. The mechanisms of the laser-induced photomechanical fragmentation are found to be rather similar in molecular and metal targets. In both cases, the relaxation of the laser-induced stresses leads to the

nucleation, growth and coalescence of voids in a subsurface region of an irradiated target. The evolution of the voids can lead to the fragmentation and ejection of large chunks of material at energy densities significantly lower than the ones needed for explosive boiling of the surface region of the target. In the simulations performed for bulk targets, the voids appear and grow at a depth defined by the competition between the tensile stresses that are increasing with depth and the decreasing thermal softening. The mechanical stability of the region subjected to the void nucleation is strongly affected by the laser heating and, in both molecular and metal targets, the depth of the void nucleation is much closer to the surface as compared with the depth where the tensile component of the pressure wave reaches its maximum value. The depth of the maximum tensile stress is close to the optical penetration depth in molecular systems, whereas in bulk Ni targets the maximum tensile stress is reached at a depth that is close to the diffusive penetration depth of the excited electrons before the electron–phonon equilibration, ~ 50 nm for Ni [35].

The values of the maximum tensile pressure that can be created in the material are also limited by the onset of the void nucleation. The maximum tensile stress increases almost linearly with fluence up to the threshold fluence for void generation and saturates and even decreases at higher fluences, as shown in Fig. 10b for metals. Similar behavior has been observed in simulations performed for molecular systems [9] as well as in photoacoustic measurements performed for aqueous media irradiated in the stress confinement regime [2]. The onset of the void nucleation not only leads to the decrease of the amplitude of the tensile stresses but also results in the increase of the time the surface region remains under tension, e.g. Fig. 2b. This observation can be also related to the appearance of a negative tail in a photoacoustic signal measured in gelatine irradiated above the threshold fluence for cavitation [3].

Large-scale MD simulations provide a unique opportunity to study the microscopic picture of void evolution in laser spallation. In particular, the void volume distributions in simulations performed for molecular systems are found to be relatively well described by a power law, $N(V) \sim V^{-\tau}$, with exponent gradually increasing (absolute value of $-\tau$ decreases) with time. Two stages can be identified in the evolution of the voids. At the first stage of void nucleation and growth, the number of voids of all sizes increases, Fig. 6a, with the largest voids appearing at a certain distance from the surface. At the second stage of void coarsening and coalescence, the number of small voids is quickly decreasing whereas the number of large voids increases, Fig. 6b, leading to the eventual percolation of the empty volume and disintegration of the surface region. A power law mass distribution has been predicted for fragmentation resulting from an interaction of a shock wave with a surface [36], as well as for the droplet size distribution in a critical point gas-liquid-phase transition [37, 38]. The cluster size distributions in a recent computational study of laser ablation are found to be relatively well described by a power law with exponents different for small and large clusters [11]. A power law void volume distribution has been also reported in a MD simulation of back spallation in a metal film subjected to a high-velocity impact [39]. Interestingly, the

critical power law exponents predicted for the gas-liquid-phase transition at the critical point, $\tau \sim 2-2.5$ [37, 38], for shock-induced fragmentation, $\tau \sim 2$ [36], and observed for void distribution in MD simulations of back spallation, $\tau \sim 2.2$ [39], are close to the one observed in our simulations of laser spallation of a molecular solid at a time of 50 ps. As discussed above, at this time the character of void evolution changes from the initial regime of void nucleation and growth to the regime of void coarsening and percolation. A good agreement of the results obtained for the evolution of photomechanical damage with earlier results for shock-induced back spallation suggests that the observed processes of void nucleation, growth and coalescence may reflect general characteristics of the dynamic fracture at high deformation rates.

A comparison of the simulation results obtained for Ni films of two different thicknesses and bulk Ni targets suggests that the size/shape of the target can play an important role in laser spallation. Reflection of the compressive pressure wave from the back surface of a finite-size target results in the appearance of a second tensile wave that intersects with the tensile wave propagating from the front surface, generating maximum tensile stresses in the region of the intersection. The location of the intersection of the two tensile waves depends on the size of the film and affects the character of the spallation process. As the size of the film increases, the region of the intersection of the two tensile waves shifts farther away from the irradiated surface, where material is colder and can support higher tensile stresses. The location of the spallation region and the region of the maximum tensile stresses are splitting apart and the threshold fluence for spallation increases with thickness of the target, as illustrated in Figs. 8–11. Note that, although the details of the spallation process (e.g. the exact number and location of spallation layers and voids) vary in simulations performed for the same system and the same irradiation conditions, the general characteristics of the spallation process discussed above (the location of the regions of void nucleation and growth, the characteristics of the void size distribution and its evolution with time) are well reproducible in the simulations.

In all simulations of laser spallation of crystalline targets performed so far, a fast melting of the surface region precedes the void nucleation and spallation. The melting process, occurring under conditions of stress confinement, acts in accord with thermoelastic stresses and contributes to the buildup of the initial compressive stresses in the target. For the model EAM Ni material, the value of volume change upon melting at zero pressure is found to be $\Delta V_{\mathrm{m}} = 0.46 \, \mathrm{cm}^3/\mathrm{mole}$ and is slightly decreasing with increasing pressure [18]. The effect of melting can have an opposite effect in materials having a negative volume change of melting, such as silicon. The melting also changes the dynamic strength of the material as well as the mechanisms of the void nucleation and growth. Note that recent observation of the destruction of a solid film subjected to an instantaneous heating [29] may be related to the fact that a pair Lennard–Jones potential was used in these simulations. As mentioned above, in Sect. 4, pair potentials tend to underestimate the ratio between the cohesive energy and the energy density needed to induce melting in metals.

The ejection of a ~ 25 nm-thick liquid layer from a bulk Ni target (Fig. 11) may be related to the experimental observation of optical interference patterns or Newton rings [40]. Decomposition of the ejected liquid layer into droplets/clusters with sizes smaller than the laser wavelength would turn the ejected liquid layer into a transparent region with relatively well-defined optically flat interfaces, which is required for generation of the interference patterns.

The maximum values of the laser-induced stresses and the contribution of photomechanical effects to the onset of laser damage and spallation are related to the condition of the stress confinement discussed in the Introduction. For molecular systems, in which the heat conduction is relatively slow, the condition for stress confinement is mainly defined by the laser penetration depth, L_{p}, the laser pulse duration, τ_{p}, and the time of thermalization of the deposited laser energy, τ_{th}. It can be written for molecular systems as $\max\left\{\tau_{\mathrm{p}}, \tau_{\mathrm{th}}\right\} \leq \tau_{\mathrm{s}} \sim L_{\mathrm{p}}/C_{\mathrm{s}}$. In metals, the strength of the electron–phonon coupling and much faster electron heat conduction are additional factors that affect the maximum thermoelastic pressure that can be created in the target. The characteristic time of the energy transfer from the excited hot electrons to the lattice, $\tau_{\mathrm{e-ph}}$ (~ 5 ps for Ni [18]), and the diffusive penetration depth of the excited electrons before the electron–phonon equilibration, L_{c} (~ 50 nm for Ni [35]), define the condition for the stress confinement, $\max\{\tau_{\mathrm{p}}, \tau_{\mathrm{e-ph}}\} \leq \tau_{\mathrm{s}} \sim L_{\mathrm{c}}/C_{\mathrm{s}}$. For example, in simulations performed for 50 nm gold films [18], a weaker electron–phonon coupling increases the characteristic time of the energy transfer from the excited electrons to the lattice as compared with nickel films. Most of the energy is transferred to the lattice within $\tau_{\mathrm{e-ph}} \approx 15$ ps, whereas complete equilibration between the hot electrons and the lattice takes up to 50 ps [18]. The effective penetration depth of the excited electrons is defined for gold targets by both ballistic and diffusive energy transport and can be estimated to be $L_{\mathrm{c}} \approx 680$ nm, well above the thickness of the films studied in the simulations. The relevant size parameter in the condition for stress confinement is, therefore, the thickness of the film rather than L_{c}. As a result, the condition for the stress confinement is not satisfied for 50 nm gold films, the laser-induced thermoelastic pressure is significantly lower as compared with the nickel films and is not sufficient to induce photomechanical disintegration. The disintegration process in the gold films is found to correspond to the explosive boiling of an overheated liquid assisted by moderate tensile stresses.

REFERENCES

1 G. Paltauf, P.E. Dyer: Chem. Rev. **103**, 487 (2003)
2 A.A. Oraevsky, S.L. Jacques, F.K. Tittel: J. Appl. Phys. **78**, 1281 (1995)
3 G. Paltauf, H. Schmidt-Kloiber: Appl. Phys. A **62**, 303 (1996)
4 D. Kim, M. Ye, C.P. Grigoropoulos: Appl. Phys. A **67**, 169 (1998)
5 I. Itzkan, D. Albagli, B.J. Banish, M. Dark, C. von Rosenberg, L.T. Perelman, G.S. Janes, M.S. Feld: AIP Conf. Proc. **288**, 491 (1994)
6 R. Cramer, R.F. Haglund, Jr., F. Hillenkamp: Int. J. Mass Spectrom. Ion Process. **169**/**170**, 51 (1997)

7 R.L. Webb, J.T. Dickinson, G.J. Exarhos: Appl. Spectrosc. **51**, 707 (1997)
8 D.E. Hare, J. Franken, D.D. Dlott: J. Appl. Phys. **77**, 5950 (1995)
9 L.V. Zhigilei, B.J. Garrison: J. Appl. Phys. **88**, 1281 (2000)
10 A.G. Zhidkov, L.V. Zhigilei, A. Sasaki, T. Tajima: Appl. Phys. A **73**, 741 (2001)
11 L.V. Zhigilei: Appl. Phys. A **76**, 339 (2003)
12 L.V. Zhigilei, E. Leveugle, B.J. Garrison, Y.G. Yingling, M.I. Zeifman: Chem. Rev. **103**, 321 (2003)
13 R.L. Webb, L.C. Jensen, S.C. Langford, J.T. Dickinson: J. Appl. Phys. **74**, 2323 (1993); *ibid*, 2338 (1993)
14 A.A. Oraevsky, R. Esenaliev, S.L. Jacques, F.K. Tittel: SPIE Proc. Series **2391**, 300 (1995)
15 A. Vogel, V. Venugopalan: Chem. Rev. **103**, 321 (2003)
16 G.I. Kanel, S.V. Razorenov, A. Bogatch, A.V. Utkin, V.E. Fortov, D.E. Grady: J. Appl. Phys. **79**, 8310 (1996)
17 S. Eliezer, E. Moshe, D. Eliezer: Laser Part. Beams **20**, 87 (2002)
18 D.S. Ivanov, L.V. Zhigilei: Phys. Rev. B **68**, 064 114 (2003)
19 D.S. Ivanov, L.V. Zhigilei: Phys. Rev. Lett. **91**, 105 701 (2003)
20 A. Miotello, R. Kelly: Appl. Phys. A **69**, S67 (1999)
21 Y. Tsuboi, K. Hatanaka, H. Fukumura, H. Masuhara: J. Phys. Chem. A **102**, 1661 (1998)
22 L.V. Zhigilei, P.B.S. Kodali, B.J. Garrison: J. Phys. Chem. B **101**, 2028 (1997); ibid. **102**, 2845 (1998)
23 L.V. Zhigilei, B.J. Garrison: Mater. Res. Soc. Symp. Proc. **538**, 491 (1999)
24 S.I. Anisimov, B.L. Kapeliovich, T.L. Perel'man: Zh. Eksp. Teor. Fiz. **66**, 776 (1974) [Sov. Phys. JETP **39**, 375 (1974)]
25 X.W. Zhou, H.N.G. Wadley, R.A. Johnson, D.J. Larson, N. Tabat, A. Cerezo, A.K. Petford-Long, G.D.W. Smith, P.H. Clifton, R.L. Martens, T.F. Kelly: Acta Mater. **49**, 4005 (2001)
26 J. Hohlfeld, S.-S. Wellershoff, J. Güdde, U. Conrad, V. Jähnke, E. Matthias: Chem. Phys. **251**, 237 (2000)
27 R.S. Dingus, R.J. Scammon: SPIE Proc. **1427**, 45 (1991)
28 D. Perez, L.J. Lewis: Phys. Rev. Lett. **89**, 255 504 (2002)
29 S.I. Anisimov, V.V. Zhakhovskii, N.A. Inogamov, K. Nishihara, A.M. Oparin, Yu.V. Petrov: Pis'ma Zh. Eksp. Teor. Fiz. **77**, 731 (2003) [JETP Lett. **77**, 606 (2003)]
30 M.S. Daw, S.M. Foiles, M.I. Baskes: Mater. Sci. Rep. **9**, 251 (1993)
31 G. Paltauf, H. Schmidt-Kloiber: Appl. Phys. A **68**, 525 (1999)
32 L.V. Zhigilei, B.J. Garrison: Appl. Surf. Sci. **127**–**129**, 142 (1998)
33 T.A. Schoolcraft, G.S. Constable, L.V. Zhigilei, B.J. Garrison: Anal. Chem. **72**, 5143 (2000)
34 A. Upadhyay, H.M. Urbassek: unpublished
35 D.S. Ivanov, L.V. Zhigilei: Appl. Phys. A, DOI 10.1007/s00339-004-2607-0
36 I.S. Bitensky, E.S. Parilis: Nucl. Instrum. Methods Phys. Res., Sect. B **21**, 26 (1987)
37 M.I. Fisher: Rep. Prog. Phys. **30**, 615 (1967)
38 H.M. Urbassek: Nucl. Instrum. Methods Phys. Res., Sect. B **31**, 541 (1988)
39 A. Strachan, T. Çağin, W.A. Goddard III: Phys. Rev. B **63**, 060 103 (2001)
40 K. Sokolowski-Tinten, J. Bialkowski, A. Cavalleri, D. von der Linde, A. Oparin, J. Meyer-ter-Vehn, S.I. Anisimov: Phys. Rev. Lett. **81**, 224 (1998)